GEOPHYSICS, VOL. 83, NO. 3 (MAY-JUNE 2018); P. S237–S248, 9 FIGS.
10.1190/GEO2017-0465.1

Check for updates

Downloaded 09/20/18 to 138.67.129.34. Redistribution subject to SEG license or copyright; see Terms of Use at http://library.seg.org/

Elastic least-squares reverse time migration using the energy norm

Daniel Rocha[1] and Paul Sava[1]

ABSTRACT

Incorporating anisotropy and elasticity into least-squares migration is an important step toward recovering accurate amplitudes in seismic imaging. An efficient way to extract reflectivity information from anisotropic elastic wavefields exploits properties of the energy norm. We derive linearized modeling and migration operators based on the energy norm to perform anisotropic least-squares reverse time migration (LSRTM) describing subsurface reflectivity and correctly predicting observed data without costly decomposition of wave modes. Imaging operators based on the energy norm have no polarity reversal at normal incidence and remove backscattering artifacts caused by sharp interfaces in the earth model, thus accelerating convergence and generating images of higher quality when compared with images produced by conventional methods. With synthetic and field data experiments, we find that our elastic LSRTM method generates high-quality images that predict the data for arbitrary anisotropy, without the complexity of wave-mode decomposition and with a high convergence rate.

INTRODUCTION

The search for more reliable seismic images and additional subsurface information, such as fracture distribution, drives advances in seismic acquisition, such as larger offsets, wider azimuths, and multicomponent recording. All of these advances facilitate incorporating anisotropy and elasticity into wavefield extrapolation and reverse time migration (RTM), which is the state-of-art wavefield imaging algorithm suitable for complex geologic structures (Baysal et al., 1983; Lailly, 1983; McMechan, 1983; Levin, 1984; Chang and McMechan, 1987; Hokstad et al., 1998; Farmer et al., 2009; Zhang and Sun, 2009). Although seismic acquisition improves with such advances, it always involves practical limitations, such as finite and irregular data sampling, which negatively impact wavefield imaging methods. Even if anisotropy and elasticity are assumed in wavefield migration, such limitations still exist. Consequently, this type of migration often leads to images with poor resolution and unbalanced illumination due to such practical acquisition constraints, even though image amplitudes are more reliable when compared with acoustic and/or isotropic imaging (Lu et al., 2009; Phadke and Dhubia, 2012; Du et al., 2014; Hobro et al., 2014).

A common solution to these limitations is the implementation of least-squares migration (LSM), which iteratively attenuates artifacts caused by truncated acquisition and provides high-quality images that best predict observed data at receiver locations in a least-squares sense (Chavent and Plessix, 1999; Nemeth et al., 1999; Kuehl and Sacchi, 2003; Aoki and Schuster, 2009; Dong et al., 2012; Yao and Jakubowicz, 2012). In particular, if the two-way wave equation is used for extrapolation, the method is called least-squares RTM (LSRTM) (Dai et al., 2010; Dai and Schuster, 2012; Dong et al., 2012; Yao and Jakubowicz, 2012). However, to overcome these issues from acquisition and to exploit the advantages of more realistic wave extrapolation, some authors propose LSRTM that accounts for multiparameter earth models that can either incorporate solely anisotropy (Huang et al., 2016), elastic (Alves and Biondi, 2016; Feng and Schuster, 2016; Xu et al., 2016; Duan et al., 2017; Ren et al., 2017), or viscosity effects (Dutta and Schuster, 2014; Sun et al., 2015). For instance, the viscoacoustic and pseudoacoustic implementations define earth reflectivity in terms of contrast from a single model parameter (Dutta and Schuster, 2014; Huang et al., 2016) or in terms of a scalar image based on conventional crosscorrelation between wavefields (Sun et al., 2015). Alternatively, elastic LSRTM implementations in isotropic media provide multiple images that are defined in terms of crosscorrelation between decomposed wave modes (Alves and Biondi, 2016; Feng and Schuster, 2016; Xu et al., 2016; Duan et al., 2017). However, wave-mode decomposition in anisotropic media is costly and not as straightforward as in isotropic media; therefore, anisotropic wave-mode decomposition remains a subject of ongoing research (Yan and Sava, 2009, 2011; Zhang and McMechan, 2010; Cheng and Fomel, 2014; Sripanich et al., 2015; Wang et al., 2016).

Manuscript received by the Editor 20 July 2017; revised manuscript received 30 October 2017; published ahead of production 14 January 2018; published online 13 April 2018.
[1]Colorado School of Mines, Center for Wave Phenomena, Golden, Colorado, USA. E-mail: drocha@mines.edu; psava@mines.edu.
© 2018 Society of Exploration Geophysicists. All rights reserved.

Downloaded 09/20/18 to 138.67.129.34. Redistribution subject to SEG license or copyright; see Terms of Use at http://library.seg.org/

Incorporating elasticity and anisotropy into LSRTM is possible with elastic wavefield imaging using the energy norm (Rocha et al., 2017). This type of imaging exploits realistic vector displacement field extrapolation within a multiparameter anisotropic and elastic earth model, and it generates scalar images of the subsurface without costly decomposition of wave modes. As opposed to more conventional imaging conditions, the elastic imaging condition based on the energy norm exhibits no polarity reversal at normal incidence, and computes an appropriate correlation between wavefields that attenuates low-wavenumber artifacts caused by waves that do not correctly characterize subsurface reflectivity (e.g., wave backscattering from salt interfaces). Such artifacts are harmful to the LSRTM inversion and retard convergence because they do not accurately characterize reflections in the subsurface. One outstanding issue with energy imaging is the physical interpretation of the scalar image; we interpret the resulting amplitudes as a measure of the collective perturbation in all earth model parameters, in contrast with more conventional images that represent either individual earth model perturbations or amplitude conversion (e.g., P into S) for different incident and reflected wave modes. As for any other wavefield migration method, its quality suffers from the acquisition limitations discussed earlier. Therefore, we define a linearized modeling operator that generates anisotropic elastic scattered wavefields, and we propose a LSRTM method that uses the energy image as a proxy for the reflectivity model. This LSRTM method is ideal to generate high-resolution images that correctly predict observed multicomponent data, without the shortcomings of different wave modes and full-wavefield phenomena present in anisotropic elastic wavefields. We demonstrate all the benefits of the method with synthetic and field data experiments.

THEORY

We can express elastic wavefield migration with mathematical operators such that

$$\mathbf{m} = \mathbf{L}^{\mathrm{T}}\mathbf{d}_r, \tag{1}$$

where $\mathbf{L}^{\mathrm{T}}$ is the migration operator, $\mathbf{d}_r$ is the single-scattered multicomponent data recorded at receiver locations, and $\mathbf{m}$ is an image or a set of images associated with the earth reflectivity. The operator $\mathbf{L}^{\mathrm{T}}$ involves backpropagation of $\mathbf{d}_r$ through an earth model generating a receiver wavefield $\mathbf{u}_r$, and the application of an imaging condition comparing $\mathbf{u}_r$ with the source wavefield $\mathbf{u}_s$ (extrapolated from a source function and location). For instance, an elastic imaging condition can involve decomposition of the wavefields $\mathbf{u}_s$ and $\mathbf{u}_r$ into separated wave modes and the application of crosscorrelation between wave modes (Yan and Sava, 2007). One generally considers wavefield migration as the adjoint operator of linearized modeling (also known as single-scattering modeling) (Claerbout, 1992). Therefore, $\mathbf{L}$ is the linearized modeling operator such that

$$\mathbf{d}_r = \mathbf{L}\mathbf{m}, \tag{2}$$

and it generates single-scattered data $\mathbf{d}_r$ at receiver locations using an image containing reflectors that act as sources under the action of the background (or source) wavefield $\mathbf{u}_s$ (embedded in the operator $\mathbf{L}$).

Energy-norm linearized modeling and migration operators

For two anisotropic elastic source and receiver wavefields that are functions of space $\mathbf{x}$ and time t, $\mathbf{u}_s(\mathbf{x}, t)$ and $\mathbf{u}_r(\mathbf{x}, t)$, we can form an image using the energy imaging condition (Rocha et al., 2017):

$$I_E(\mathbf{x}) = \sum_t [\rho\dot{\mathbf{u}}_s \cdot \dot{\mathbf{u}}_r - (\underline{\underline{\mathbf{c}}}\nabla\mathbf{u}_s) : \nabla\mathbf{u}_r], \tag{3}$$

where $\rho(\mathbf{x})$ is the density of the medium and $\underline{\underline{\mathbf{c}}}(\mathbf{x})$ is the second-order stiffness tensor. The superscript dot applied on the wavefields indicates time differentiation, and ∇ is the spatial gradient. The symbol : indicates the Frobenius product between two matrices resulting in a scalar quantity (Golub and Loan, 1996). A more compact form of equation 3 uses the so-called energy vectors that are defined as

$$\square\mathbf{u}_s = \{\rho^{1/2}\dot{\mathbf{u}}_s, -\underline{\underline{\mathbf{c}}}^{1/2}(\nabla\mathbf{u}_s)\}, \tag{4}$$

$$\square\mathbf{u}_r = \{\rho^{1/2}\dot{\mathbf{u}}_r, -\underline{\underline{\mathbf{c}}}^{1/2}(\nabla\mathbf{u}_r)\}. \tag{5}$$

Analyzing the terms in equations 4 and 5, one can note that the energy vectors contain 12 components, three from the terms $\rho^{1/2}\dot{\mathbf{u}}_{s,r}$ and nine from $\underline{\underline{\mathbf{c}}}^{1/2}(\nabla\mathbf{u}_{s,r})$. We can also define $\square$ as the energy operator containing derivatives and medium parameters applicable to a multicomponent wavefield. Using the definition of energy vectors, the imaging condition in equation 3 becomes

$$I_E = \sum_t \square\mathbf{u}_s \cdot \square\mathbf{u}_r. \tag{6}$$

To obtain the adjoint operator associated with the imaging condition in equation 6, we rewrite the expression in operator form:

$$\mathbf{m} = (\square\mathbf{u}_s)^{\mathrm{T}}\square\mathbf{u}_r. \tag{7}$$

We can write the elastic wavefields $\mathbf{u}_s$ and $\mathbf{u}_r$ in terms of a sequence of operators applied to the source function $\mathbf{d}_s$ and to the receiver data $\mathbf{d}_r$, respectively. First, we implement injection of the multicomponent source function and receiver data into the earth model by operators $\mathbf{K}_s$ and $\mathbf{K}_r$, respectively. Second, we apply forward and backward elastic wavefield extrapolation operators $\mathbf{E}_+$ and $\mathbf{E}_-$. Hence, we express the wavefields by $\mathbf{u}_s = \mathbf{E}_+\mathbf{K}_s\mathbf{d}_s$ and $\mathbf{u}_r = \mathbf{E}_-\mathbf{K}_r\mathbf{d}_r$, and we can rewrite equation 7 as

$$\mathbf{m} = (\square\mathbf{E}_+\mathbf{K}_s\mathbf{d}_s)^{\mathrm{T}}\square\mathbf{E}_-\mathbf{K}_r\mathbf{d}_r. \tag{8}$$

Equation 8 is in the form $\mathbf{m} = \mathbf{L}^{\mathrm{T}}\mathbf{d}_r$, where

$$\mathbf{L}^{\mathrm{T}} = (\square\mathbf{E}_+\mathbf{K}_s\mathbf{d}_s)^{\mathrm{T}}\square\mathbf{E}_-\mathbf{K}_r = (\square\mathbf{u}_s)^{\mathrm{T}}\square\mathbf{E}_-\mathbf{K}_r. \tag{9}$$

Therefore, this chain of operators $\mathbf{L}^{\mathrm{T}}$ represents the migration based on the energy norm. We can obtain the operator $\mathbf{L}$ (adjoint of $\mathbf{L}^{\mathrm{T}}$) if we apply the adjoint for each individual operator and reverse the order of operators:

$$\mathbf{L} = \mathbf{K}_r^{\mathrm{T}}\mathbf{E}_+\square^{\mathrm{T}}(\square\mathbf{E}_+\mathbf{K}_s\mathbf{d}_s) = \mathbf{K}_r^{\mathrm{T}}\mathbf{E}_+\square^{\mathrm{T}}\square\mathbf{u}_s, \tag{10}$$

where $\mathbf{E}_-^{\mathrm{T}} = \mathbf{E}_+$. This chain of operators $\mathbf{L}$ represents the linearized modeling based on the energy norm, involving extraction of multi-

Downloaded 09/20/18 to 138.67.129.34. Redistribution subject to SEG license or copyright; see Terms of Use at http://library.seg.org/

component single-scattered data at the receiver locations ($\mathbf{K}_r^{\mathrm{T}}$), and elastic wavefield extrapolation ($\mathbf{E}_+$) from virtual multicomponent sources computed by $\square^{\mathrm{T}}\square\mathbf{u}_s\mathbf{m}$.

To elucidate the linearized modeling based on the energy norm, here are the steps involved in computing the scattered data at receivers ($\mathbf{d}_r$):

1) Inject the source wavelet $\mathbf{d}_s$ using $\mathbf{K}_s$.
2) Extrapolate ($\mathbf{E}_+$) the injected source $\mathbf{K}_s\mathbf{d}_s$, generating the background wavefield $\mathbf{u}_s$.
3) Compute $\square\mathbf{u}_s$, a 12C vector field shown in equation 4.
4) Multiply each component of $\square\mathbf{u}_s$ by the scalar reflectivity model $\mathbf{m}$.
5) Compute $\square^{\mathrm{T}}\square\mathbf{u}_s\mathbf{m}$, a 3C virtual source field.
6) Extrapolate ($\mathbf{E}_+$) the virtual source $\square^{\mathrm{T}}\square\mathbf{u}_s\mathbf{m}$, generating the scattered wavefield $\mathbf{u}_r$.
7) Extract data at receiver locations $\mathbf{d}_r$ by applying $\mathbf{K}_r^{\mathrm{T}}$ to the scattered wavefield.

In Appendix A, we represent all individual operators involved in $\mathbf{L}$ and $\mathbf{L}^{\mathrm{T}}$ pictorially to illustrate the series of increases and reductions in dimensionality throughout our linearized modeling and migration. In addition, in Appendix B, we show all the components of the virtual source term $\square^{\mathrm{T}}\square\mathbf{u}_s\mathbf{m}$ explicitly for a 2D vertical transversely isotropic (VTI) medium.

Physical interpretation of energy imaging operators

For arbitrary anisotropy, we can write the energy linearized source term explicitly as

$$\mathbf{f}(\mathbf{x},t) = [\rho\ddot{\mathbf{u}}_s - \nabla\cdot(\underline{\underline{\mathbf{c}}}\nabla\mathbf{u}_s)]\frac{\delta m}{m}, \tag{11}$$

where $\mathbf{f}(\mathbf{x},t)$ is a displacement field and $(\delta m/m)(\mathbf{x})$ is the medium perturbation capturing contributions for all earth model parameters. Notice that the terms $\rho\ddot{\mathbf{u}}_s$ and $\nabla\cdot(\underline{\underline{\mathbf{c}}}\nabla\mathbf{u}_s)$ have the units of force per volume:

$$\rho\ddot{\mathbf{u}}_s(\text{mass}\times\text{acceleration/volume}), \tag{12}$$

$$\nabla\cdot(\underline{\underline{\mathbf{c}}}\nabla\mathbf{u}_s)(\text{pressure/distance}), \tag{13}$$

and $(\delta m/m)$ is the dimensionless. Therefore, the linearized source is proportional to the force generated by the energy terms from the background wavefield and to the distribution of the collective perturbation of the earth model. The imaging condition in equation 3, which is the adjoint operation of the proposed linearized modeling, delivers an image representing the relative contribution of all earth model perturbations ($\delta m/m$). Linearized modeling can also be implemented in terms of individual perturbations from each earth model parameter, and in this case, the linearized source is written as

$$\mathbf{f}(\mathbf{x},t) = \ddot{\mathbf{u}}_s\delta\rho - \nabla\cdot(\delta\underline{\underline{\mathbf{c}}}\nabla\mathbf{u}_s). \tag{14}$$

By defining linearized modeling in terms of individual earth model perturbations, equation 14 is analogous to the Born source defined in adjoint-state methods for wavefield tomography (Tarantola, 1988; Tromp et al., 2005; Zhu et al., 2009).

If we assume a fixed perturbation $\delta m/m$ in all model parameters, we can obtain equation 11 as in Born approximation, i.e., small perturbation in the earth model parameters generating a single-scattered wavefield. The elastic-wave equation for an anisotropic medium is

$$\rho_0\ddot{\mathbf{u}}_s = \nabla\cdot(\underline{\underline{\mathbf{c}}}_0\nabla\mathbf{u}_s). \tag{15}$$

Without loss of generality, for the following discussion, we simplify it to the isotropic elastic-wave equation:

$$\rho_0\ddot{\mathbf{u}}_s = \lambda_0[\nabla(\nabla\cdot\mathbf{u}_s)] + \mu_0[\nabla\cdot(\nabla\mathbf{u}_s + \nabla\mathbf{u}_s^{\mathrm{T}})], \tag{16}$$

where $\lambda_0(\mathbf{x})$ and $\mu_0(\mathbf{x})$ are the background Lamé model parameters (Aki and Richards, 2002) and $\rho_0(\mathbf{x})$ is the background density. The Born approximation involves the addition of a weak-scattered wavefield $\delta\mathbf{u}_s(\mathbf{x},t)$ generated by small perturbations in the background earth model parameters. Writing such perturbations as fixed relative increments in all parameters, we have

$$\rho = \rho_0(1+\delta m/m), \tag{17}$$

$$\lambda = \lambda_0(1+\delta m/m), \tag{18}$$

$$\mu = \mu_0(1+\delta m/m). \tag{19}$$

To simplify notation, we can omit the denominator in $\delta m/m$ for the following equations. We express the wave equation with the total wavefield (background plus scattered) as

$$\begin{aligned}(1+\delta m)\rho_0(\ddot{\mathbf{u}}_s+\ddot{\delta\mathbf{u}}_s) = {}&(1+\delta m)\lambda_0[\nabla(\nabla\cdot\mathbf{u}_s)+\nabla(\nabla\cdot\delta\mathbf{u}_s)]\\ &+(1+\delta m)\mu_0[\nabla\cdot(\nabla\mathbf{u}_s+\nabla\mathbf{u}_s^{\mathrm{T}})\\ &+\nabla\cdot(\nabla\delta\mathbf{u}_s+\nabla\delta\mathbf{u}_s^{\mathrm{T}})].\end{aligned} \tag{20}$$

Subtracting equation 16 from equation 20, and ignoring higher-order terms involving the product of δm with $\delta\mathbf{u}_s$, we obtain

$$\begin{aligned}\rho_0\ddot{\delta\mathbf{u}}_s - \lambda_0[\nabla(\nabla\cdot\delta\mathbf{u}_s)] - \mu_0[\nabla\cdot(\nabla\delta\mathbf{u}_s+\nabla\delta\mathbf{u}_s^{\mathrm{T}})] = {}&\\ -\delta m\{\rho_0\ddot{\mathbf{u}}_s - \lambda_0[\nabla(\nabla\cdot\mathbf{u}_s)] - \mu_0[\nabla\cdot(\nabla\mathbf{u}_s+\nabla\mathbf{u}_s^{\mathrm{T}})]\},&\end{aligned} \tag{21}$$

which means that the perturbed wavefield $\delta\mathbf{u}_s$ is generated using the right side of equation 21 as the source term $\mathbf{f}(\mathbf{x},t)$. The energy linearized modeling (equation 21) and the energy imaging condition that delivers δm can be written in operator form. We write these operators a function of the individual model parameters for a 2D isotropic medium in Appendix C.

Energy-norm elastic LSM

The linearized modeling operator $\mathbf{L}$ and its adjoint enables us to compute an image that minimizes the objective function:

$$E(\mathbf{m}) = \frac{1}{2}\|\mathbf{L}\mathbf{m} - \mathbf{d}_r\|^2. \tag{22}$$

The reflectivity that minimizes equation 22 is mathematically described as

$$\mathbf{m}^{\mathrm{LS}} = (\mathbf{L}^{\mathrm{T}}\mathbf{L})^{-1}\mathbf{L}^{\mathrm{T}}\mathbf{d}_r. \tag{23}$$

However, to find $\mathbf{m}^{\mathrm{LS}}$, one generally uses iterative methods that exploit the gradient of the objective function in equation 22. For a linear problem, such as LSRTM, the conjugate gradient algorithm is generally used (Hestenes and Stiefel, 1952; Scales, 1987). The gradient of the objective function in equation 22 with respect to a model at a given iteration i is

$$\mathbf{g}_i = \frac{\partial E(\mathbf{d}, \mathbf{m}_i)}{\partial \mathbf{m}_i} = \mathbf{L}^{\mathrm{T}}(\mathbf{L}\mathbf{m}_i - \mathbf{d}_r). \tag{24}$$

The model update at each iteration can be a scaled version of the gradient, or ideally can incorporate an approximation of the Hessian operator $\mathbf{H} = (\mathbf{L}^{\mathrm{T}}\mathbf{L})$ (Aoki and Schuster, 2009; Tang, 2009; Dai et al., 2010):

$$\mathbf{m}_{i+1} = \mathbf{m}_i - \mathbf{H}^{-1}\mathbf{g}_i. \tag{25}$$

For all numerical experiments shown in this paper, we set the initial model to be zero and apply an illumination compensation on the gradient at every iteration. This illumination compensation computed from the wavefields is considered to be an approximation of the Hessian operator and act as a preconditioner for each iteration of the conjugate-gradient algorithm (Rickett, 2003; Plessix and Mulder, 2004; Du et al., 2012). We use the energy norm of the source wavefield at every spatial location as our illumination compensation factor:

$$\mathbf{h}(\mathbf{x}) = \|\mathbf{u}_s\|_E^2 = \Box\mathbf{u}_s \cdot \Box\mathbf{u}_s. \tag{26}$$

EXAMPLES

The following numerical examples demonstrate how the linearized modeling and migration operators based on the energy norm behave during LSRTM. First, we perform an experiment with a sin-

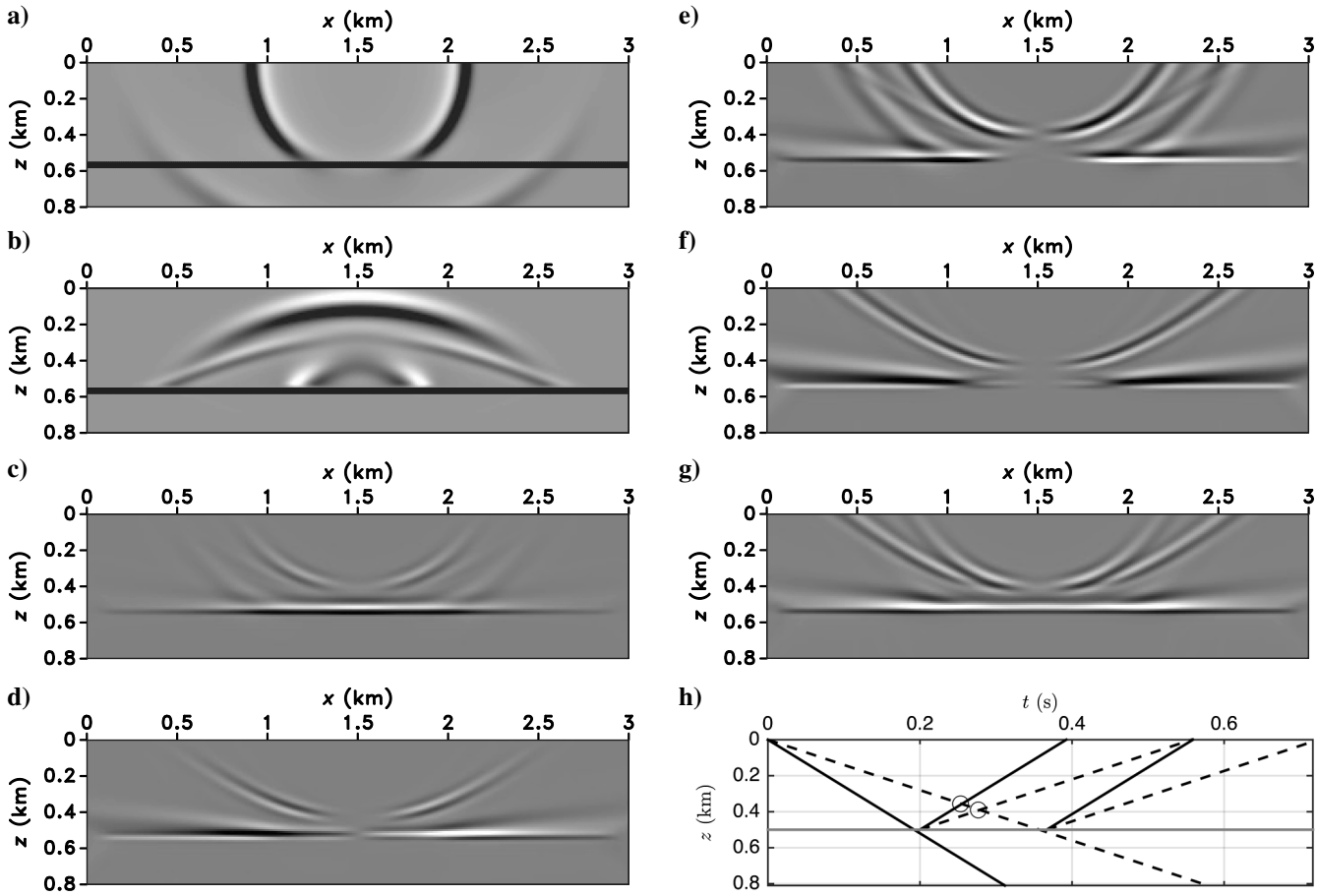


Figure 1. Snapshots of the vertical components of (a) background and (b) scattered wavefields at $t = 0.52$ s. The black line at $z = 0.55$ km indicates the position of the reflector. Using the scattered wavefield in place of the receiver wavefield, we obtain (c) PP-, (d) PS-, (e) SP-, (f) SS-, and (g) energy images. The incomplete wave-mode decomposition creates artifacts in PP-, PS-, SP-, and SS-images, and crosstalk correlation creates artifacts in all images. The space-time diagram in (h) shows all wave events associated with this experiment: The solid and dashed lines indicate P- and S-waves, respectively, and the horizontal gray line indicates the reflector. With this diagram, we can note that (e) SP- and (f) SS-images contain additional crosstalk artifacts due to the correlation of the incident S-wave with the decomposed PP- and PS-reflections, respectively, as seen by the intersections between these events indicated by the unfilled circles in the diagram.

Downloaded 09/20/18 to 138.67.129.34. Redistribution subject to SEG license or copyright; see Terms of Use at http://library.seg.org/

Downloaded 09/20/18 to 138.67.129.34. Redistribution subject to SEG license or copyright; see Terms of Use at http://library.seg.org/

gle flat reflector to convey some intuition about how the method works; second, we show an experiment using a realistic synthetic earth model containing many reflectors and structures to test the method in more complex geologic settings with sharp interfaces that create backscattering artifacts in conventional imaging methods; finally, we validate the method by applying it to a North Sea field data set.

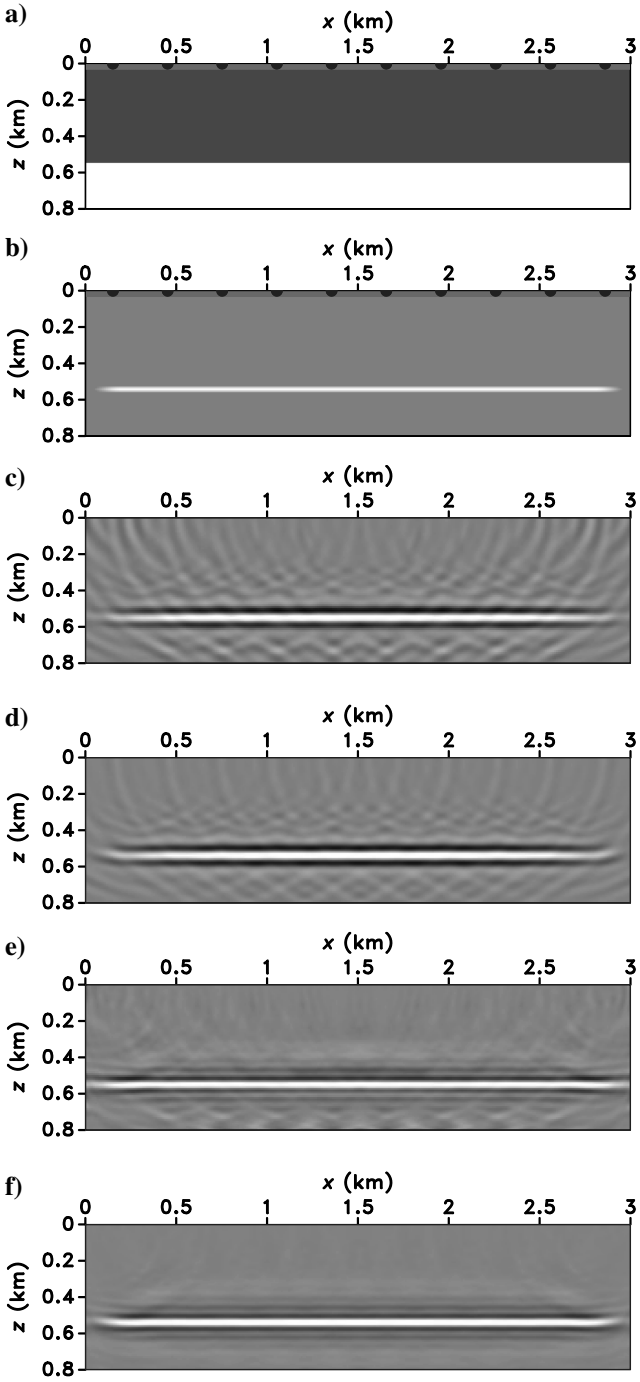


Figure 2. (a) Density model used in full-wavefield modeling and (b) reflectivity model used in linearized modeling. The acquisition geometry consists of 10 sources and a line of receivers (black dots and gray line at the top). Elastic energy RTM image with (c) full-modeled data and with (d) linearized-modeled data. Elastic energy LSRTM image with (e) full-modeled data and with (f) linearized-modeled data. Note how LSRTM attenuates artifacts caused by sparse acquisition.

Single-reflector linearized modeling

We use a constant background earth model and a simple reflectivity model (containing one flat reflector) to show an example of a scattered wavefield obtained by the energy linearized modeling and to compare the quality of the energy imaging condition with its conventional counterparts, which are based on wave-mode decomposition and generate PP-, PS-, SP-, and SS-images (Yan and Sava, 2008). The parameters of the background earth model are $\rho = 2.5$ g/cm^3, $V_{P0} = 2.2$ km/s (P-wave velocity along the symmetry axis), $V_{S0} = 1.3$ km/s (S-wave velocity along the symmetry axis), and Thomsen parameters $\epsilon = 0.4$ and $\delta = 0.3$ (Thomsen, 1986). The source is located at $x = 1.5$ km at the surface and con-

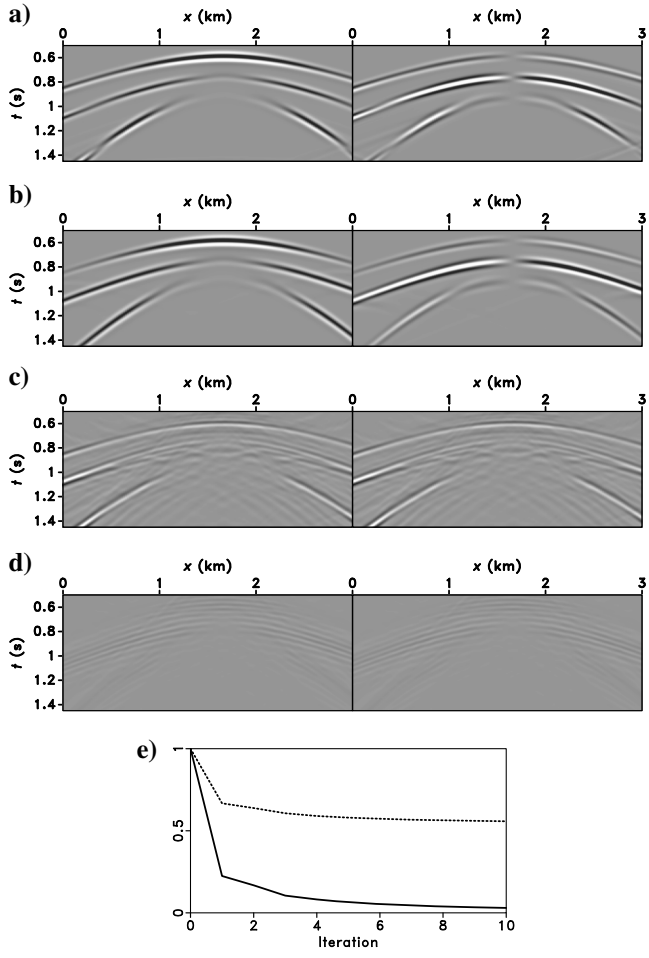


Figure 3. Vertical- (left) and horizontal- (right) component data from (a) full modeling and (b) linearized modeling. Data residuals from the LSRTM images using (c) full modeling and from (d) linearized modeling. (e) Normalized objective functions for inversion using full-modeled data (dashed) and linearized data (solid). The far-offset amplitudes from full-modeled data are not correctly predicted by the linearized modeling operator.

Downloaded 09/20/18 to 138.67.129.34. Redistribution subject to SEG license or copyright; see Terms of Use at http://library.seg.org/

sists of a vertical displacement force that generates P- and S-waves, as seen in Figure 1a. The source (or background) wavefield interacts with the reflectivity model at $z = 0.55$ km and generates the scattered wavefield shown in Figure 1b, in which we can observe PP (first event, top to bottom), PS (second), and SP (third) reflections. At a later time, the linearized modeling also generates an SS reflection. As these figures indicate, the proposed linearized modeling procedure generates a multicomponent scattered wavefield that contains only primary reflection events. Nonreflection events such as head waves are not generated as they would be with full-wavefield modeling.

With the extrapolated wavefields, we generate energy and conventional images (Figure 1c–1g). Although the scattered wavefield is not generated from the receiver locations, we use it in place of the receiver wavefield in all imaging conditions. We make this choice such that the computed images do not contain artifacts caused by acquisition geometry and by fake events generated with backpropagation of injected displacement at receiver locations. Also, because the background earth model is constant, no backscattering artifacts exist in this experiment. The remaining artifacts are considered crosstalk artifacts caused not by reflections, but instead by the interaction between different wave modes. For background and scattered wavefields extrapolated for all times, we compute the Helmholtz decomposition and obtain PP-, PS-, SP-, and SS-images. Because the earth model is VTI, Helmholtz decomposition does not fully separate wave modes and causes crosstalk artifacts for all images due to some residual in the decomposed modes. Although the energy image (Figure 1g) does not involve wave-mode decomposition, it exhibits crosstalk artifacts that are similar in amplitude from the ones in the conventional images. As stated elsewhere (Rocha et al., 2017), the energy imaging condition only attenuates events from source and receiver wavefields that share the same propagation and polarization directions, which is not the case for crosstalk between different wave modes from source and receiver wavefields. The space-time diagram in Figure 1h shows all the wave events related to this experiment, and indicates two crosstalk correlations that are independent of wave-mode decomposition. Such correlations are caused by the slower incident S-wave that interacts with the faster PP- and PS-reflections, generating artifacts in SP- and SS-images, respectively.

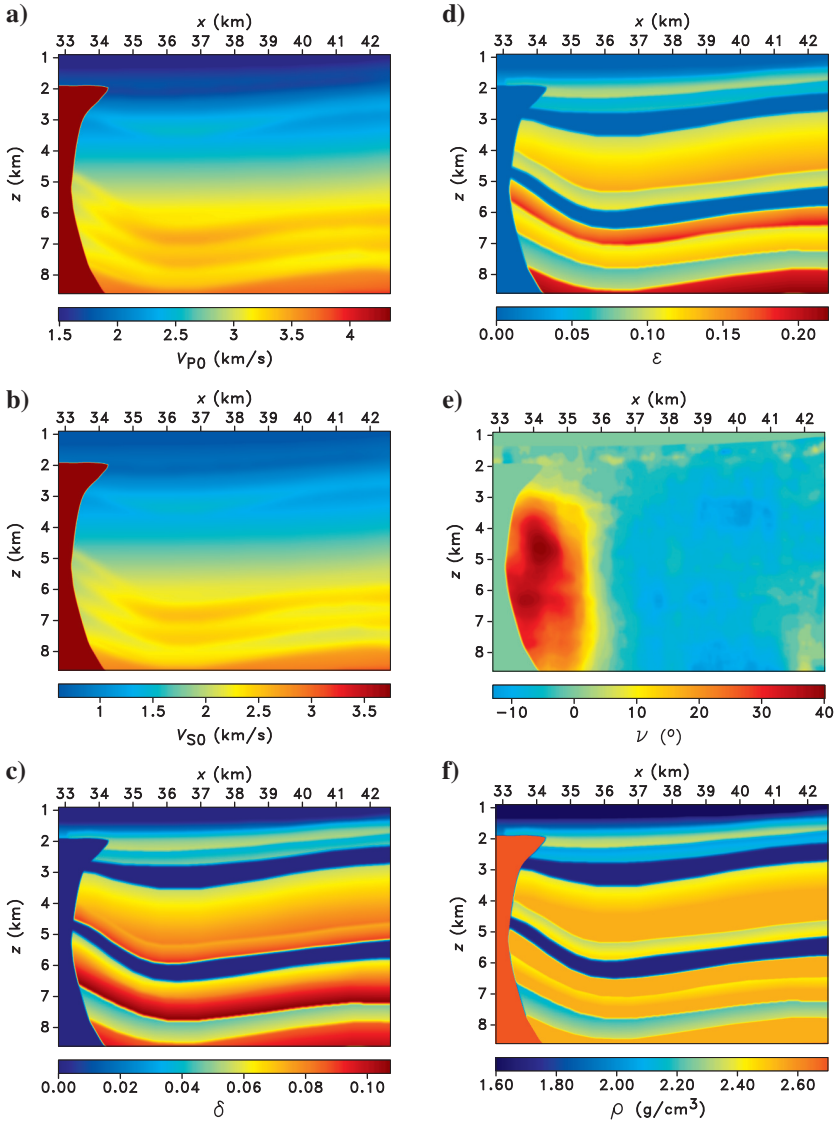


Figure 4. The BP TTI model parameters: (a) P-wave and (b) S-wave velocities along the symmetry axis; Thomsen parameters (c) δ and (d) ε along the symmetry axis; (e) tilt of the symmetry axis (ν); and (f) density with contrasts for full-wavefield modeling experiment.

Single-reflector LSRTM

We demonstrate energy-based LSRTM using the same earth model from the previous simple experiment but with a contrast at the reflector location. The reflector consists of the following contrasts: $\Delta\rho = 0.7$ g/cm^3, $\Delta V_{P0} = 0.6$ km/s, and $\Delta V_{S0} = 0.5$ km/s. Figure 2a shows the density model and the acquisition geometry that consists of 10 sources and a line of receivers at the surface. We create a scalar reflectivity based on the contrast of the earth model (Figure 2b). We generate shot records by two different methods: (1) full-wavefield modeling that uses the earth model with contrasts as conventionally implemented to generate synthetic elastic data and (2) linearized modeling based on the energy norm, which applies the operator in equation 10 to the reflectivity from Figure 2b using the background earth model (without contrast). We migrate both synthetic data sets using the energy imaging condition. Figure 2c and 2d shows the stacked energy RTM images that use the full-modeled data and linearized-modeled data, respectively. We also compute 10 iterations of energy LSRTM for both data sets: Figure 2e and 2e shows the final stacked LSRTM images that use the full-modeled data and linearized-modeled data, respectively. By comparing the LSRTM images with their RTM counterparts,

Downloaded 09/20/18 to 138.67.129.34. Redistribution subject to SEG license or copyright; see Terms of Use at http://library.seg.org/

one can observe the better quality of the LSRTM images: The artifacts caused by the truncated acquisition are attenuated, and the amplitudes are closer to the true reflectivity.

One can note that the RTM and LSRTM images using the linearized-modeled data have fewer artifacts than the ones using the full-modeled data. To explain why, we show both synthetic data sets in Figure 3a and 3b. From early to late arrival times, the three visible events in each data set correspond to (1) P-P (apex approximately $t = 0.6$ s), (2) P-S/S-P (apex approximately $t = 0.8$ s), and (3) S-S reflections (apex approximately $t = 0.9$ s). For the near offsets, we notice that events in both data sets match in phase and polarity because only specular reflections exist at these near offsets. However, because the linearized modeling is a simplification of full-wavefield modeling, it can only predict single-scattering events and cannot predict wave phenomena that are beyond the critical angle, such as head waves, and these phenomena influence the amplitude of the three events at the far offsets of Figure 3a. One can also notice such behavior on the data residuals at iteration 10 (Figure 3c and 3d). The linearized modeling embedded in the engine of both LSRTM results can only predict amplitude from reflections events, and it cannot match the far-offset amplitudes from the full-modeled data (Figure 3c). Alternatively, by using the same linearized modeling operator to generate synthetic data, the data residual (Figure 3d) and its related objective function (Figure 3e) decrease substantially more and are close to zero at the last iteration, because our operators are proper adjoints of each other, and can perfectly match the data set containing only reflections after several iterations.

2007 BP tilted transversely isotropic anisotropic benchmark model

We use a portion of the 2007 BP tilted transversely isotropic (TTI) benchmark model to test the method in a more complicated synthetic model. The original model consists of V_{P0}, ϵ, δ, and the tilt of the symmetry axis at every point (ν); we create V_{S0} and ρ from V_{P0} (Figure 4). The experiment geometry consists of 55 pressure sources equally spaced in the water at the surface ($z = 0.092$ km) and a line of multicomponent receivers at every grid point at the water bottom, which varies between the depths of $z = 1.0$ km and $z = 1.4$ km. Similarly to the preceding example, we generate two different data sets by (1) full-wavefield modeling, using the density model with contrasts (Figure 4f) and (2) linearized modeling, using a constant density model and the reflectivity model in Figure 5e to generate reflections. All other earth model parameters are kept the same between the two experiments.

We obtain energy RTM and LSRTM images using linearized-modeled data (Figure 5a and 5c) and full-modeled data (Figure 5b and 5d). We apply a power gain with depth on the RTM images for a fair comparison with LSRTM images, because RTM images commonly have weaker amplitudes for greater depths and these amplitudes can easily be compensated by such gain. Notice that artifacts in the shallow part (mainly caused by the limited acquisition) are attenuated, and the deep reflectors as well as the salt flanks are better illuminated in the LSRTM images compared with their RTM counterparts. Both LSRTM images contain sharper reflectors and are closer to the assumed true reflectivity models shown in Figure 5e and 5f. For the LSRTM images, one can observe low-wavenumber artifacts inside the salt because most of the waves in this region do not scatter toward the receivers due to this particular experiment, which images only one side of the salt body. These events create artifacts that accumulate over iterations, and they are part of the null space for the inversion; i.e., they do not predict any reflections in the observed data. Although such artifacts do not represent actual reflectors, they are not harmful to the inversion process because they reside in the null space of the reflectivity model and do not mask any reflectors inside the salt body.

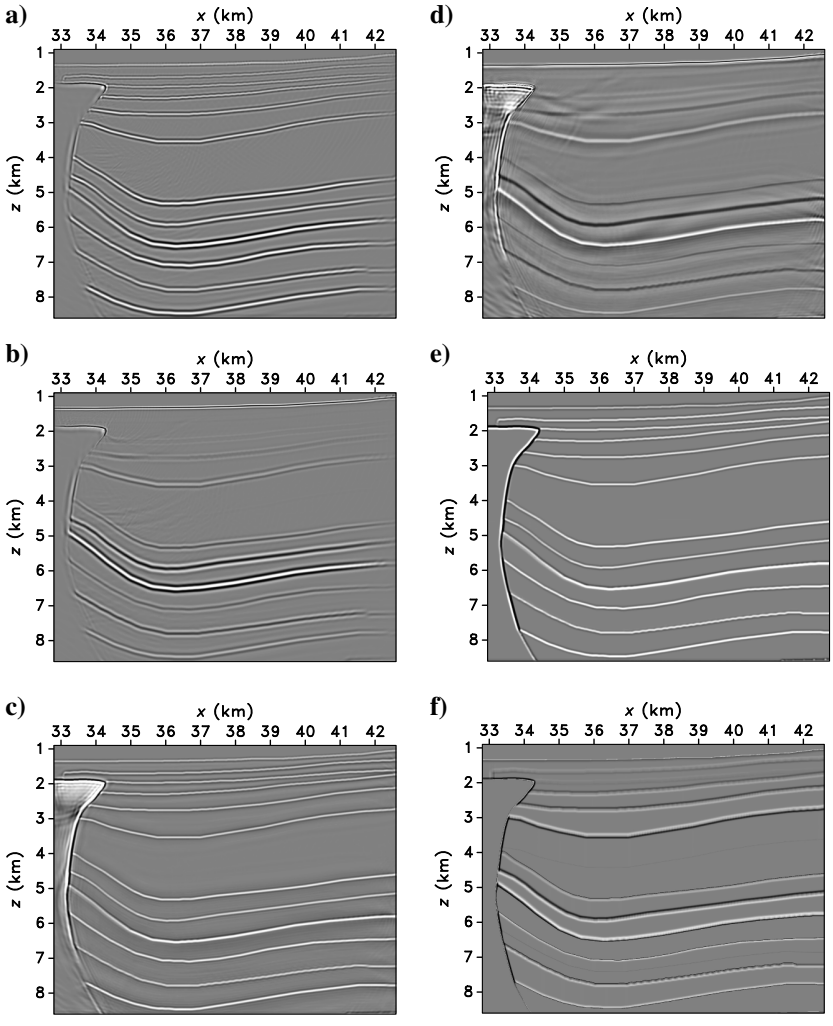


Figure 5. The RTM images using (a) linearized-modeled data and (b) full-modeled data. LSRTM images after 20 iterations using (c) linearized-modeled data and (d) full-modeled data. (e) True reflectivity model for linearized-modeled data and (f) Laplacian operator applied on the density model in Figure 4f to show contrasts that create reflections in the full-wavefield modeling.

Downloaded 09/20/18 to 138.67.129.34. Redistribution subject to SEG license or copyright; see Terms of Use at http://library.seg.org/

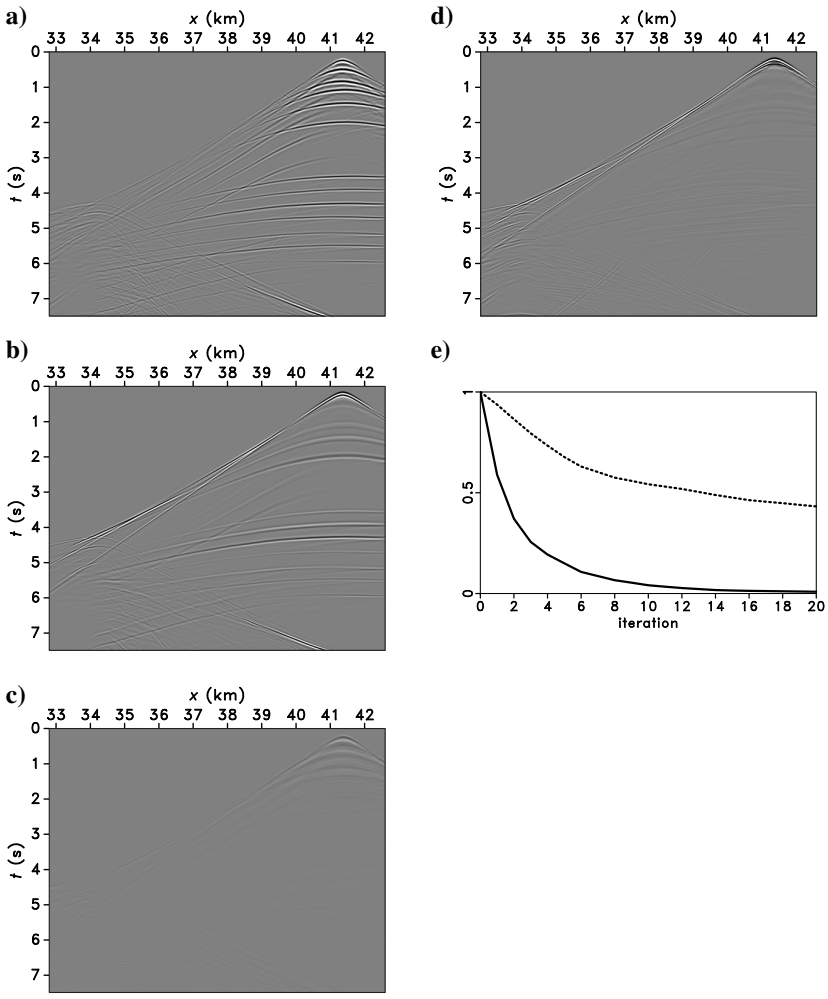


Figure 6. Vertical component of observed data at a $x_s = 41.4$ km obtained by (a) linearized modeling using the reflectivity model in Figure 5e, and (b) full-wavefield modeling using density model in Figure 4f. Vertical component data residuals after 20 iterations for (c) linearized and (d) full-wavefield modeling experiments. (e) Normalized objective function for experiments using (dashed) full-modeled and (solid) linearized data.

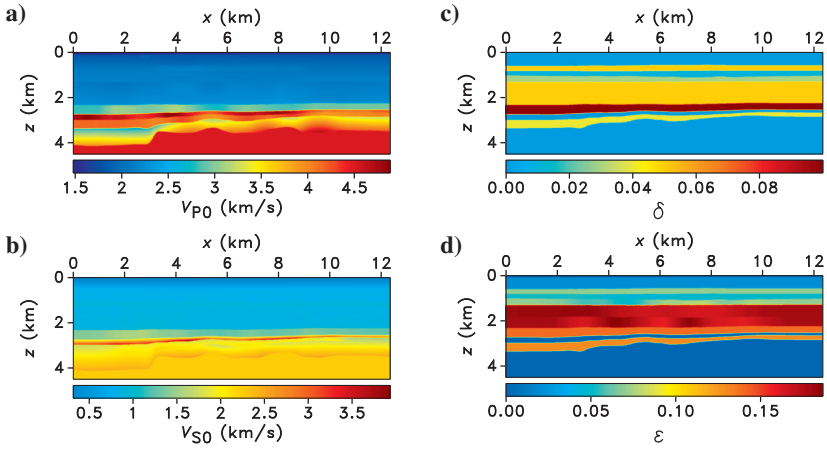


Figure 7. Volve 2D model parameters: (a) P-wave and (b) S-wave velocities along the vertical symmetry axis; Thomsen parameters (c) δ and (d) ε.

In Figure 6a and 6b, we show the observed data at a particular shot location ($x = 41.4$ km) containing offsets up to 8 km for linearized and full-wavefield modeling, respectively. The corresponding data residuals after 20 iterations are shown in Figure 6c and 6d, which are diminished when compared with the original data sets. The objective functions for both experiments are shown in Figure 6e. As expected, the objective function for the inversion using the data set generated with the linearized modeling operator itself converges to zero because our migration and modeling operators are proper adjoints of each other. The objective function for the experiment with full-modeled data decreases substantially and can potentially decrease more if more iterations are allowed because the objective function at iteration 20 retains a significant slope, as shown in Figure 6e. However, we expect the rate of convergence to be smaller over iterations until the objective function reaches a plateau because our modeling operator cannot predict events beyond single scattering in full-modeled data. In addition, differently from the single-reflector preceding example, several reflectors in this earth model cause multiple scattering events during full-wavefield modeling that are also not predicted by our linearized modeling operator. All events that exist in the data and are not predicted by our operator might form artifacts in the image, such as for any other migration methods applied on data that contains multiple reflections, turning waves, etc.

Volve ocean-bottom-cable real data set

We apply the method to a field data set acquired by an ocean-bottom cable in the Volve field, located in the North Sea (Szydlik et al., 2007). Although the original data set is three dimension, we use a 2D section near the central crossline to reduce the computational cost. The earth model is elastic VTI, and the corresponding parameters are shown in Figure 7. The prominent layer at approximately $z = 3$ km is a chalk layer that corresponds to the hydrocarbon reservoir (Szydlik et al., 2007). The data set provided was preprocessed to retain only the downgoing pressure component, and a particular common-shot gather for a source at $x = 6.3$ km is shown in Figure 8a. We obtain energy RTM and LSRTM images after 15 iterations, shown in Figure 9a and 9b, and the corresponding objective function in Figure 8d. The LSRTM image exhibits more detailed reflectors compared with the RTM image, and it enhances the amplitudes at the edges of the model. With a smooth muting of far-offset events, the objective function decreases substantially reaching 40% of its initial

Downloaded 09/20/18 to 138.67.129.34. Redistribution subject to SEG license or copyright; see Terms of Use at http://library.seg.org/

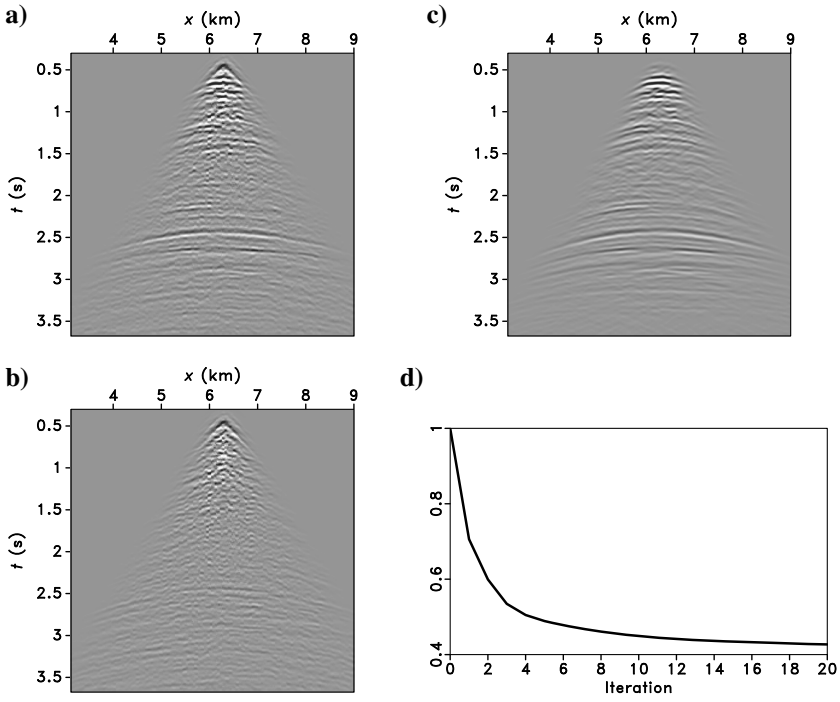


Figure 8. Volve experiment: (a) observed, (b) residual, and (c) modeled (after 15 iterations) pressure shot gathers for a source at $x = 6.4$ km. The main reflections are correctly predicted by our modeling operator. (c) Normalized objective function for LSRTM.

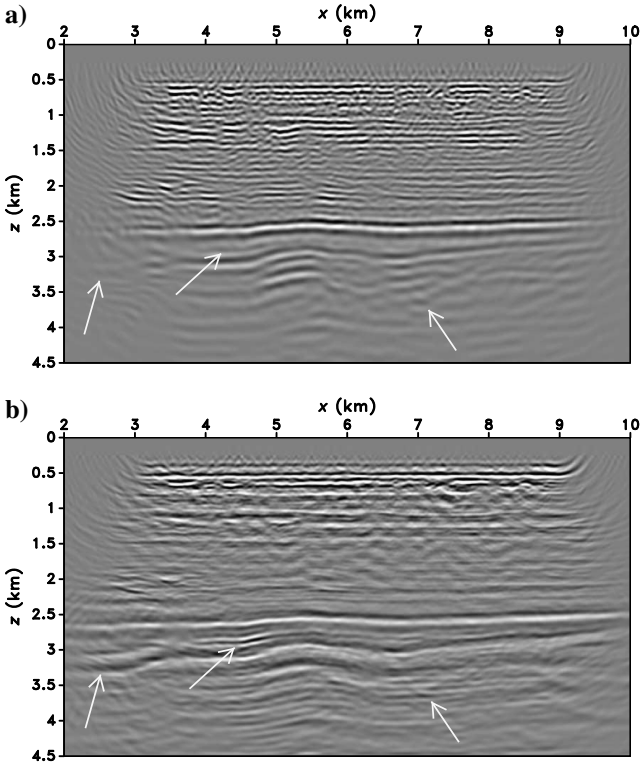


Figure 9. Volve experiment: energy (a) RTM and (b) LSRTM images. Reflectors approximately $z = 3.0$ km become sharper, especially at the edges of the image. The arrows indicate reflectors that become more visible in the LSRTM image relative to RTM.

value at the last iteration. By comparing the modeled data and residual at the last iteration (Figure 8c and 8b), and the observed data (Figure 8a), one can note that our linearized modeling operator and the image at the last iteration predict the main reflections and do not predict events such as noise, direct arrival, and far-offset amplitudes

CONCLUSION

We propose an elastic LSRTM method that uses imaging operators based on the energy norm and delivers a scalar image that contains attenuated artifacts and explains data at receiver locations. The absence of strong backscattering artifacts in our results shows the advantage of our migration operator compared with its conventional counterparts. The obtained scalar image represents the collective contribution of all perturbations in earth model parameters. Using displacement fields directly and without costly wave-mode decomposition, our linearized modeling operator generates multicomponent data sets with a scalar reflectivity that correctly predicts the amplitude and phase of the reflections in observed data, as illustrated by the final modeled data and objective functions from our numerical examples. As for any other linearized modeling procedure, events that are not reflections are inaccurately predicted by our linearized operator, and these events show in the image as artifacts. Future work involves application of our method to another multicomponent field data set that contains vertical and horizontal displacement components, and to 3D earth models.

ACKNOWLEDGMENTS

We thank the sponsors of the Center for Wave Phenomena, whose support made this research possible. We acknowledge H. Shah and BP Exploration Operation Company Limited for creating the TTI model. We are grateful to Statoil ASA and the Volve license partners ExxonMobil E&P Norway AS and Bayerngas Norge AS for the release of the Volve data. We would like to thank M. Houbiers at Statoil for helping us with the Volve data set. The authors appreciate the constructive comments from the anonymous reviewers of this paper. We acknowledge A. Guitton for helpful discussions. The synthetic examples in this paper use the Madagascar open-source software package (Fomel et al., 2013) freely available from http://www.ahay.org.

Downloaded 09/20/18 to 138.67.129.34. Redistribution subject to SEG license or copyright; see Terms of Use at http://library.seg.org/

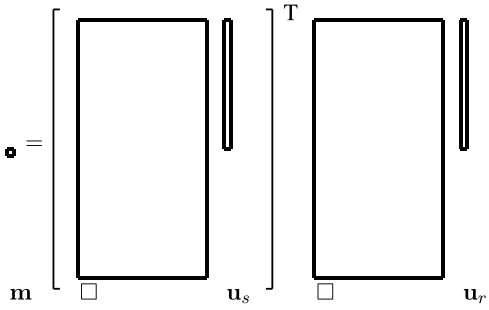
APPENDIX A

ENERGY-BASED MODELING AND MIGRATION OPERATORS

The energy image $\mathbf{m}(\mathbf{x})$ is obtained by the expression:

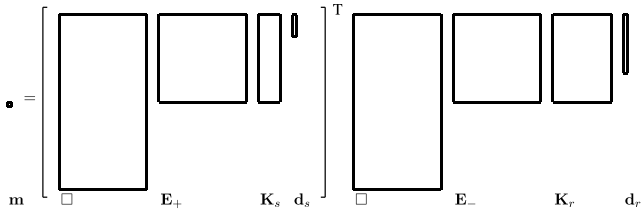
$$\mathbf{m} = (\square \mathbf{u}_s)^{\mathrm{T}} \square \mathbf{u}_r, \tag{A-1}$$

which can be schematically represented as



The operator $\square$ turns a 3C displacement field into a 12C vector field that contains spatial and temporal derivatives. Equation A-1 also implies summation over time. We represent this increase in dimensions pictorially by making the matrix of $\square$ considerably larger than the wavefield vectors $\mathbf{u}_s$ and $\mathbf{u}_r$. Using extrapolator and injection operators, as explained in the body of the paper, we have

$$\mathbf{m} = (\square \mathbf{E}_+ \mathbf{K}_s \mathbf{d}_s)^{\mathrm{T}} \square \mathbf{E}_- \mathbf{K}_r \mathbf{d}_r. \tag{A-2}$$



In compact form, we can rewrite equation A-2 as

$$\mathbf{m} = \mathbf{L}^{\mathrm{T}} \mathbf{d}_r. \tag{A-3}$$

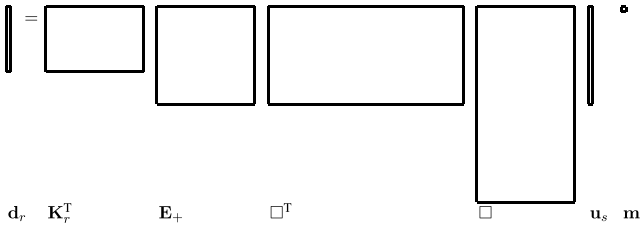
Linearized modeling is defined as

$$\mathbf{d}_r = \mathbf{L}\mathbf{m}. \tag{A-4}$$

Based on equation A-2, we can rewrite equation A-4 as

$$\mathbf{d}_r = \mathbf{K}_r^{\mathrm{T}} \mathbf{E}_-^{\mathrm{T}} \square^{\mathrm{T}} \square \mathbf{u}_s \mathbf{m}, \tag{A-5}$$

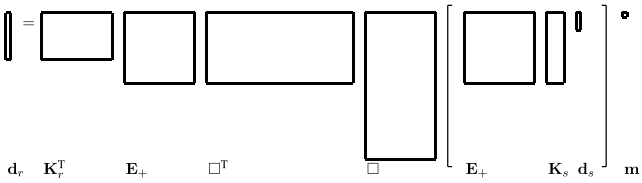
which is represented schematically as



or

$$\mathbf{d}_r = \mathbf{K}_r^{\mathrm{T}} \mathbf{E}_+ \square^{\mathrm{T}} \square (\mathbf{E}_+ \mathbf{K}_s \mathbf{d}_s) \mathbf{m} \tag{A-6}$$

represented as



The virtual multicomponent source computed for the generation of the scattered wavefield is represented by the chain of operators $\square^{\mathrm{T}} \square (\mathbf{E}_+ \mathbf{K}_s \mathbf{d}_s) \mathbf{m} = \square^{\mathrm{T}} \square \mathbf{u}_s \mathbf{m}$.

APPENDIX B

MULTICOMPONENT VIRTUAL SOURCE FOR 2D VTI LINEARIZED MODELING

We can write the energy imaging condition (equation 3) for a 2D VTI medium in matrix notation as

$$I_E(\mathbf{x}) = \rho \begin{bmatrix} \dot{U}_1^s & \dot{U}_3^s \end{bmatrix} \begin{bmatrix} \dot{U}_1^r \\ \dot{U}_3^r \end{bmatrix} - \begin{bmatrix} C_{11} U_{1,1}^s + C_{13} U_{3,3}^s & C_{55}(U_{1,3}^s + U_{3,1}^s) \\ C_{55}(U_{1,3}^s + U_{3,1}^s) & C_{33} U_{3,3}^s + C_{13} U_{1,1}^s \end{bmatrix} : \begin{bmatrix} U_{1,1}^r & U_{3,1}^r \\ U_{1,3}^r & U_{3,3}^r \end{bmatrix}, \tag{B-1}$$

where $U_{i,j}^{s,r}$ is the jth derivative of the ith component of wavefield $\mathbf{u}_s$ or $\mathbf{u}_r$, and C_{ij} are the stiffness coefficients in Voigt notation (Helbig, 1994). The symbol: represents Frobenius product between two matrices: an element-wise product between matrices with the corresponding sum of the products resulting in a scalar. Indices $i, j = \{1, 2, 3\}$ refer to $\{x, y, z\}$. The superscript dot on $U_i^{s,r}$ indicates the time differentiation. Rewriting all derivatives applied to U^r as operators, we obtain

$$I_E = \rho \begin{bmatrix} \dot{U}_1^s & \dot{U}_3^s \end{bmatrix} \begin{bmatrix} D_t & 0 \\ 0 & D_t \end{bmatrix} \begin{bmatrix} U_1^r \\ U_3^r \end{bmatrix} - \begin{bmatrix} C_{11} U_{1,1}^s + C_{13} U_{3,3}^s & C_{55}(U_{1,3}^s + U_{3,1}^s) \\ C_{55}(U_{1,3}^s + U_{3,1}^s) & C_{33} U_{3,3}^s + C_{13} U_{1,1}^s \end{bmatrix} : \begin{bmatrix} D_1 & 0 \\ 0 & D_3 \end{bmatrix} \begin{bmatrix} U_1^r & U_3^r \\ U_1^r & U_3^r \end{bmatrix}, \tag{B-2}$$

Downloaded 09/20/18 to 138.67.129.34. Redistribution subject to SEG license or copyright; see Terms of Use at http://library.seg.org/

where D_t, D_1, and D_3 indicate the derivative operators in time, x, and z, respectively. Therefore, the application of the energy imaging condition can be considered as an operator acting on the receiver wavefield $[\,U_1^r \quad U_3^r\,]$. Its adjoint operator (linearized modeling) acts on the image (or reflectivity) I_E:

$$[f_1\ f_3]=\left[\begin{bmatrix} D_t^{\mathrm{T}} & 0 \\ 0 & D_t^{\mathrm{T}} \end{bmatrix}\begin{bmatrix} \cdot U_1^s \\ \cdot U_3^s \end{bmatrix}\rho I_E\right]^{\mathrm{T}} - \begin{bmatrix} D_1^{\mathrm{T}} & D_3^{\mathrm{T}} \end{bmatrix}\begin{bmatrix} C_{11}U_{1,1}^s+C_{13}U_{3,3}^s & C_{55}(U_{1,3}^s+U_{3,1}^s) \\ C_{55}(U_{1,3}^s+U_{3,1}^s) & C_{33}U_{3,3}^s+C_{13}U_{1,1}^s \end{bmatrix} I_E, \tag{B-3}$$

where $[\,f_1 \quad f_3\,]$ is a 2C virtual source that generates the scattered wavefield $[\,U_1^r \quad U_3^r\,]$. We can rewrite the expression for each component individually for such a virtual source:

$$\begin{aligned} f_1(\mathbf{x},t) = {} & D_t^{\mathrm{T}}\rho D_t U_1^s I_E \\ & - D_1^{\mathrm{T}}[C_{11}D_1U_1^s + C_{13}D_3U_3^s]I_E \\ & - D_3^{\mathrm{T}}[C_{55}(D_3U_1^s + D_1U_3^s)]I_E, \end{aligned} \tag{B-4}$$

$$\begin{aligned} f_3(\mathbf{x},t) = {} & D_t^{\mathrm{T}}\rho D_t U_3^s I_E \\ & - D_1^{\mathrm{T}}[C_{55}(D_3U_1^s + D_1U_3^s)]I_E \\ & - D_3^{\mathrm{T}}[C_{33}D_3U_3^s + C_{13}D_1U_1^s]I_E. \end{aligned} \tag{B-5}$$

Therefore, we can consider the generation of the energy scattered wavefield in an elastic 2D VTI medium as the extrapolation of a virtual multicomponent source defined in equations B-4 and B-5.

APPENDIX C

PERTURBATION OF MODEL PARAMETERS IN ENERGY MIGRATION AND LINEARIZED MODELING

For a 2D isotropic medium, images representing perturbations for each earth model parameter can be written as

$$\begin{bmatrix} \delta\rho \\ \delta\lambda \\ \delta\mu \end{bmatrix} = \mathbf{M}\begin{bmatrix} U_1^r \\ U_3^r \end{bmatrix}, \tag{C-1}$$

where

$$\mathbf{M} = \begin{bmatrix} \rho\dot{U}_1^s D_t & \rho\dot{U}_3^s D_t \\ -\lambda(U_{1,1}^s + U_{3,3}^s)D_1 & -\lambda(U_{1,1}^s + U_{3,3}^s)D_3 \\ -\mu[2U_{1,1}^s D_1 + (U_{1,3}^s + U_{3,1}^s)D_3] & -\mu[2U_{3,3}^s D_3 + (U_{1,3}^s + U_{3,1}^s)D_1] \end{bmatrix}. \tag{C-2}$$

Here, we use the same notation for the operators from Appendix B. This type of images based on model perturbations are used in other LSRTM implementations (Alves and Biondi, 2016; Feng and Schuster, 2016; Xu et al., 2016; Duan et al., 2017; Ren et al., 2017) and conform with adjoint-state tomography (Tarantola, 1988; Tromp et al., 2005; Zhu et al., 2009). We can invoke the summation of the model perturbations using a stacking operator $[1 \quad 1 \quad 1]$ such that

$$\delta m = [\,1 \quad 1 \quad 1\,]\begin{bmatrix} \delta\rho \\ \delta\lambda \\ \delta\mu \end{bmatrix} = [\,1 \quad 1 \quad 1\,]\mathbf{M}\begin{bmatrix} U_1^r \\ U_3^r \end{bmatrix}. \tag{C-3}$$

Applying the stacking operator to left and right sides of equation C-3 yields

$$\begin{aligned} \delta m &= \delta\rho + \delta\lambda + \delta\mu \\ &= \begin{bmatrix} \rho\dot{U}_1^s D_t - \lambda(U_{1,1}^s + U_{3,3}^s)D_1 - \mu[2U_{1,1}^s D_1 + (U_{1,3}^s + U_{3,1}^s)D_3] \\ \rho\dot{U}_3^s D_t - \lambda(U_{1,1}^s + U_{3,3}^s)D_3 - \mu[2U_{3,3}^s D_3 + (U_{1,3}^s + U_{3,1}^s)D_1] \end{bmatrix}^{\mathrm{T}}\begin{bmatrix} U_1^r \\ U_1^r \end{bmatrix}. \end{aligned} \tag{C-4}$$

Equation C-4 represents the summation of the perturbation images, and it is equivalent to the energy imaging condition for a 2D isotropic medium. Its adjoint, energy linearized modeling, is expressed as

$$\begin{bmatrix} f_1 \\ f_3 \end{bmatrix} = \begin{bmatrix} D_t^{\mathrm{T}}\cdot U_1^s\rho - D_1^{\mathrm{T}}(U_{1,1}^s + U_{3,3}^s)\lambda - [2D_1^{\mathrm{T}}U_{1,1}^s + D_3^{\mathrm{T}}(U_{1,3}^s + U_{3,1}^s)]\mu \\ D_t^{\mathrm{T}}\cdot U_3^s\rho - D_3^{\mathrm{T}}(U_{1,1}^s + U_{3,3}^s)\lambda - [2D_3^{\mathrm{T}}U_{3,3}^s + D_1^{\mathrm{T}}(U_{1,3}^s + U_{3,1}^s)]\mu \end{bmatrix}\delta m, \tag{C-5}$$

which can be rewritten in terms of individual model parameters and the stacking operator:

$$\begin{bmatrix} f_1 \\ f_3 \end{bmatrix} = \begin{bmatrix} D_t^{\mathrm{T}}\cdot U_1^s\rho - D_1^{\mathrm{T}}(U_{1,1}^s + U_{3,3}^s)\lambda - [2D_1^{\mathrm{T}}U_{1,1}^s + D_3^{\mathrm{T}}(U_{1,3}^s + U_{3,1}^s)]\mu \\ D_t^{\mathrm{T}}\cdot U_3^s\rho - D_3^{\mathrm{T}}(U_{1,1}^s + U_{3,3}^s)\lambda - [2D_3^{\mathrm{T}}U_{3,3}^s + D_1^{\mathrm{T}}(U_{1,3}^s + U_{3,1}^s)]\mu \end{bmatrix}[\,1 \quad 1 \quad 1\,]\begin{bmatrix} \delta\rho \\ \delta\lambda \\ \delta\mu \end{bmatrix}, \tag{C-6}$$

or in terms of a spraying operator (adjoint of stacking) and the adjoint of $\mathbf{M}$:

$$\begin{bmatrix} f_1 \\ f_3 \end{bmatrix} = \mathbf{M}^{\mathrm{T}}\begin{bmatrix} 1 \\ 1 \\ 1 \end{bmatrix}\delta m. \tag{C-7}$$

REFERENCES

Aki, K., and P. G. Richards, 2002, Quantitative seismology, 2nd ed.: University Science Books.

Alves, G., and B. Biondi, 2016, Imaging condition for elastic reverse time migration: 86th Annual International Meeting, SEG, Expanded Abstracts, 3959–3965.

Aoki, N., and G. T. Schuster, 2009, Fast least-squares migration with a deblurring filter: Geophysics, **74**, no. 6, WCA83–WCA93, doi: 10.1190/1.3155162.

Baysal, E., D. D. Kosloff, and J. W. C. Sherwood, 1983, Reverse time migration: Geophysics, **48**, 1514–1524, doi: 10.1190/1.1441434.

Chang, W.-F., and G. A. McMechan, 1987, Elastic reverse-time migration: Geophysics, **52**, 1365–1375, doi: 10.1190/1.1442249.

Chavent, G., and R.-E. Plessix, 1999, An optimal true-amplitude least-squares prestack depth-migration operator: Geophysics, **64**, 508–515, doi: 10.1190/1.1444557.

Cheng, J., and S. Fomel, 2014, Fast algorithms for elastic-wave-mode separation and vector decomposition using low-rank approximation for anisotropic media: Geophysics, **79**, no. 4, C97–C110, doi: 10.1190/geo2014-0032.1.

Claerbout, J. F., 1992, Earth soundings analysis: Processing versus inversion: Blackwell Scientific Publications.

Dai, W., C. Boonyasiriwat, and G. Schuster, 2010, 3D multisource least-squares reverse-time migration: 80th Annual International Meeting, SEG, Expanded Abstracts, 3120–3124.

Dai, W., and G. T. Schuster, 2012, Plane-wave least-squares reverse time migration: 82nd Annual International Meeting, SEG, Expanded Abstracts, doi: 10.1190/segam2012-0382.1.

Dong, S., J. Cai, M. Guo, S. Suh, Z. Zhang, B. Wang, and Z. Li, 2012, Least-squares reverse time migration: Towards true amplitude imaging

and improving the resolution: 82nd Annual International Meeting, SEG, Expanded Abstracts, doi: 10.1190/segam2012-1488.1.
Du, Q., M. Zhang, G. Fang, X. Gong, and C. Guo, 2014, Relatively amplitude-preserved ADCIGs based on elastic RTM by modifying the initial condition as the boundary condition: 84th Annual International Meeting, SEG, Expanded Abstracts, 1888–1893.
Du, X., R. Fletcher, E. Mobley, and E. Yarman, 2012, Source and receiver illumination compensation for reverse-time migration: 74th Annual International Conference and Exhibition, EAGE, Extended Abstracts, doi: 10.3997/2214-4609.20148793.
Duan, Y., P. Sava, and A. Guitton, 2017, Elastic least-squares reverse time migration: Geophysics, **82**, no. 4, S315–S325, doi: 10.1190/geo2016-0564.1.
Dutta, G., and G. T. Schuster, 2014, Attenuation compensation for least-squares reverse time migration using the viscoacoustic-wave equation: Geophysics, **79**, no. 6, S251–S262, doi: 10.1190/geo2013-0414.1.
Farmer, P., Z. Z. Zhou, and D. Jones, 2009, The role of reverse time migration in imaging and model estimation: The Leading Edge, **28**, 436–441, doi: 10.1190/1.3112761.
Feng, Z., and G. T. Schuster, 2016, Elastic least-squares reverse time migration: 86th Annual International Meeting, SEG, Expanded Abstracts, 3959–3965.
Fomel, S., P. Sava, I. Vlad, Y. Liu, and V. Bashkardin, 2013, Madagascar: Open-source software project for multidimensional data analysis and reproducible computational experiments: Journal of Open Research Software, **1**, e8, doi: 10.5334/jors.ag.
Golub, G. H., and C. F. V. Loan, 1996, Matrix computations, 3rd ed.: John Hopkins University Press.
Helbig, K., 1994, Foundations of anisotropy for exploration seismics: Elsevier Science Serials.
Hestenes, M. R., and E. Stiefel, 1952, Methods of conjugate gradients for solving linear systems: Journal of Research of the National Bureau of Standards, **49**, 409–436, doi: 10.6028/jres.049.044.
Hobro, J. W. D., C. H. Chapman, and J. O. A. Robertsson, 2014, A method for correcting acoustic finite-difference amplitudes for elastic effects: Geophysics, **79**, no. 4, T243–T255, doi: 10.1190/geo2013-0335.1.
Hokstad, K., R. Mittet, and M. Landrø, 1998, Elastic reverse time migration of marine walkaway vertical seismic profiling data: Geophysics, **63**, 1685–1695, doi: 10.1190/1.1444464.
Huang, J., D. Si, Z. Li, and J. Huang, 2016, Plane-wave least-squares reverse time migration in complex VTI media: 86th Annual International Meeting, SEG, Expanded Abstracts, 441–446.
Kuehl, H., and M. D. Sacchi, 2003, Least-squares wave-equation migration for AVO/AVA inversion: Geophysics, **68**, 262–273, doi: 10.1190/1.1543212.
Lailly, P., 1983, The seismic inverse problem as a sequence of before stack migrations: Proceedings of the Conference on Inverse Scattering, Theory and Application, SIAM, 206–220.
Levin, S. A., 1984, Principle of reverse-time migration: Geophysics, **49**, 581–583, doi: 10.1190/1.1441693.
Lu, R., P. Traynin, and J. E. Anderson, 2009, Comparison of elastic and acoustic reverse-time migration on the synthetic elastic Marmousi-II OBC dataset: 79th Annual International Meeting, SEG, Expanded Abstracts, 2799–2803.
McMechan, G. A., 1983, Migration by extrapolation of time dependent boundary values: Geophysical Prospecting, **31**, 413–420, doi: 10.1111/j.1365-2478.1983.tb01060.x.
Nemeth, T., C. Wu, and G. T. Schuster, 1999, Least-squares migration of incomplete reflection data: Geophysics, **64**, 208–221, doi: 10.1190/1.1444517.
Phadke, S., and S. Dhubia, 2012, Reverse time migration of marine models with elastic wave equation and amplitude preservation: 82nd Annual International Meeting, SEG, Expanded Abstracts, doi: 10.1190/segam2012-1107.1.
Plessix, R., and W. Mulder, 2004, Frequency-domain finite-difference amplitude-preserving migration: Geophysical Journal International, **157**, 975–987, doi: 10.1111/j.1365-246X.2004.02282.x.
Ren, Z., Y. Liu, and M. K. Sen, 2017, Least-squares reverse time migration in elastic media: Geophysical Journal International, **208**, 1103–1125, doi: 10.1093/gji/ggw443.
Rickett, J. E., 2003, Illumination-based normalization for wave-equation depth migration: Geophysics, **68**, 1371–1379, doi: 10.1190/1.1598130.
Rocha, D., N. Tanushev, and P. Sava, 2017, Anisotropic elastic wavefield imaging using the energy norm: Geophysics, **82**, no. 3, S225–S234, doi: 10.1190/geo2016-0424.1.
Scales, J., 1987, Tomographic inversion via the conjugate gradient method: Geophysics, **52**, 179–185, doi: 10.1190/1.1442293.
Sripanich, Y., S. Fomel, J. Sun, and J. Cheng, 2015, Elastic wave-vector decomposition in orthorhombic media: 85th Annual International Meeting, SEG, Expanded Abstracts, 498–503.
Sun, J., S. Fomel, and T. Zhu, 2015, Preconditioning least-squares RTM in viscoacoustic media by Q-compensated RTM: 85th Annual International Meeting, SEG, Expanded Abstracts, 3959–3965.
Szydlik, T., P. Smith, S. Way, L. Aamodt, and C. Friedrich, 2007, 3D PP/PS prestack depth migration on the Volve field: First Break, **25**, 43–47.
Tang, Y., 2009, Target-oriented wave-equation least-squares migration/inversion with phase-encoded hessian: Geophysics, **74**, no. 6, WCA95–WCA107, doi: 10.1190/1.3204768.
Tarantola, A., 1988, Theoretical background for the inversion of seismic waveforms including elasticity and attenuation: Pure and Applied Geophysics, **128**, 365–399, doi: 10.1007/BF01772605.
Thomsen, L., 1986, Weak elastic anisotropy: Geophysics, **51**, 1954–1966, doi: 10.1190/1.1442051.
Tromp, J., C. Tape, and Q. Liu, 2005, Seismic tomography, adjoint methods, time reversal and banana-doughnut kernels: Geophysical Journal International, **160**, 195–216, doi: 10.1111/j.1365-246X.2004.02453.x.
Wang, W., G. A. McMechan, C. Tang, and F. Xie, 2016, Up/down and P/S decompositions of elastic wavefields using complex seismic traces with applications to calculating Poynting vectors and angle-domain common-image gathers from reverse time migrations: Geophysics, **81**, no. 4, S181–S194, doi: 10.1190/geo2015-0456.1.
Xu, L., A. Stanton, and M. D. Sacchi, 2016, Elastic least squares reverse time migration: 86th Annual International Meeting, SEG, Expanded Abstracts, 3959–3965.
Yan, J., and P. Sava, 2007, Elastic wavefield imaging with scalar and vector potentials: 77th Annual International Meeting, SEG, Expanded Abstracts, 2150–2154.
Yan, J., and P. Sava, 2008, Isotropic angle-domain elastic reverse-time migration: Geophysics, **73**, no. 6, S229–S239, doi: 10.1190/1.2981241.
Yan, J., and P. Sava, 2009, Elastic wave-mode separation for VTI media: Geophysics, **74**, no. 5, WB19–WB32, doi: 10.1190/1.3184014.
Yan, J., and P. Sava, 2011, Elastic wave-mode separation for tilted transverse isotropy media: Geophysical Prospecting, **60**, 29–48, doi: 10.1111/j.1365-2478.2011.00964.x.
Yao, G., and H. Jakubowicz, 2012, Least-squares reverse-time migration: 82nd Annual International Meeting, SEG, Expanded Abstracts, doi: 10.1190/segam2012-1425.1.
Zhang, Q., and G. A. McMechan, 2010, 2D and 3D elastic wavefield vector decomposition in the wavenumber domain for VTI media: Geophysics, **75**, no. 3, D13–D26, doi: 10.1190/1.3431045.
Zhang, Y., and J. Sun, 2009, Practical issues in reverse time migration: True amplitude gathers, noise removal and harmonic source encoding: First Break, **27**, 53–59, doi: 10.3997/1365-2397.2009002.
Zhu, H., Y. Luo, T. Nissen-Meyer, C. Morency, and J. Tromp, 2009, Elastic imaging and time-lapse migration based on adjoint methods: Geophysics, **74**, no. 6, WCA167–WCA177, doi: 10.1190/1.3261747.

Downloaded 09/20/18 to 138.67.129.34. Redistribution subject to SEG license or copyright; see Terms of Use at http://library.seg.org/